Title	Surprising increase in yield stress of Mg single crystal using long-period stacking ordered nanoplates
Author(s)	Hagihara, Koji; Ueyama, Ryohei; Yamasaki, Michiaki et al.
Citation	Acta Materialia. 2021, 209, p. 116797
Version Type	VoR
URL	https://hdl.handle.net/11094/89785
rights	This article is licensed under a Creative Commons Attribution 4.0 International License.
Note	

Acta Materialia 209 (2021) 116797

Contents lists available at ScienceDirect

Acta Materialia

journal homepage: www.elsevier.com/locate/actamat

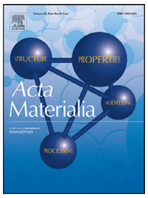

Surprising increase in yield stress of Mg single crystal using long-period stacking ordered nanoplates

Koji Hagihara[a,*], Ryohei Ueyama[a], Michiaki Yamasaki[b], Yoshihito Kawamura[b], Takayoshi Nakano[a]

[a] *Division of Materials and Manufacturing Science, Graduate School of Engineering, Osaka University, 2-1 Yamadaoka, Suita, Osaka 565-0871, Japan*
[b] *Magnesium Research Center & Department of Materials Science, Kumamoto University, 2-39-1 Kurokami, Chuo-ku, Kumamoto 860-8555, Japan*

ARTICLE INFO

Article history:
Received 23 September 2020
Revised 7 January 2021
Accepted 6 March 2021
Available online 13 March 2021

Keywords:
Mg alloy
Strength
LPSO-phase
Microstructure
Nanoplate

ABSTRACT

Mg–Zn–Y ternary alloys containing the long-period stacking ordered (LPSO) phase exhibit superior mechanical properties. This is believed to be originating from the LPSO phase acting as the strengthening phase. However, we first clarify that the mechanical properties of the matrix Mg solid solution in the Mg/LPSO two-phase alloy are significantly different from those of pure Mg. The yield stress of a $Mg_{99.2}Zn_{0.2}Y_{0.6}$ single crystal (matrix Mg solid solution) is almost the same as that of an LPSO single-phase alloy. This is ascribed to the formation of thin stacking-fault-like defects, named “LPSO nanoplate”. In $Mg_{99.2}Zn_{0.2}Y_{0.6}$, kink-band formation is induced in the same manner as that in the LPSO phase in deformation, resulting in high strength accompanied with increased ductility. Our results suggest that the strengthening mechanism of the Mg/LPSO two-phase alloy must be reconsidered depending on the microstructure. Furthermore, the results suggest that new ultrahigh-strength Mg alloys, which have much lower Zn and Y contents but the mechanical properties are comparable or superior than the present Mg/LPSO two-phase alloys, are expected to be developed via the appropriate control of LPSO nanoplate microstructures.

1. Introduction

There is an increased demand for the development of new lightweight structural materials to overcome issues related to global warming. Mg alloys are a potential candidate for addressing these issues. However, there are serious drawbacks for expanding the use of Mg alloys in many fields of application—notably, their insufficient strength and low corrosion resistance. Commercial cast Mg alloys exhibit a low tensile yield strength of ~100–250 MPa and limited ductility (elongation: 3%–15%) at room temperature [1]. In order to improve these properties, Mg alloys containing the long-period stacking ordered (LPSO) phase have recently received attention [2–15]. The LPSO phase is known to form in Mg–Zn–Y ternary alloys. The LPSO phase has an approximate composition of Mg–5at% Zn–7at% Y in the typical Mg/LPSO two-phase alloy with a composition of $Mg_{97}Zn_1Y_2$. The crystal structure of the LPSO phase is constructed by the long-period stacking—typically, 18- or 14-fold—of close-packed planes (the basal plane in hexagonal systems) along the *c* axis [16,17]. Additionally, the Y/Zn atoms in the LPSO phase are periodically segregated into four specific layers of close-packed planes where a face-centered cubic (fcc)-like stacking fault exists [17], as illustrated in Supplementary Fig. S1. Kawamura et al. first reported that a rapidly solidified Mg/LPSO two-phase alloy with a composition of $Mg_{97}Zn_1Y_2$, which contains the ~24 vol% of LPSO phase, exhibits an extremely high yield stress of ~600 MPa while retaining ~5% elongation [2]. Further, a high ultimate tensile strength of ~400 MPa can be obtained for extruded alloys fabricated by a simpler process [5]. To clarify the physical origin of this drastic strengthening, the mechanical properties of the LPSO phase have been extensively studied. Hagihara et al. examined the mechanical properties of the LPSO phase by using a directionally solidified (DS) LPSO single-phase crystal [18–20]. As a result, the plastic deformation behavior of the LPSO phase was found to have strong anisotropy. Basal slip can be operative in the LPSO phase, similar to Mg, and is accompanied by a low yield stress. However, in the case where stress is applied parallel to the basal plane, the yield stress is quite high and different from that in Mg; this is because the formation of deformation twins is prohibited, which is ascribed to the complicated LPSO structure [18]. Instead, unique kink bands are formed, resulting in ductility [18–20]. A kink band

---

[*] Corresponding author.
E-mail address: hagihara@mat.eng.osaka-u.ac.jp (K. Hagihara).

https://doi.org/10.1016/j.actamat.2021.116797
1359-6454/

is a deformation band in which basal dislocations are aligned along a direction perpendicular to the slip plane [18–25], as illustrated in Supplemental Fig. S2. More recently, it was found that the formed kink bands act as effective obstacles to the motion of basal dislocations, contributing to the strengthening of the LPSO phase (kink-band strengthening) [26,27].

In contrast, the mechanical properties of the matrix Mg phase in Mg/LPSO two-phase alloys have not received as much attention from researchers. The composition of the Mg matrix phase [3] is approximately Mg–0.2at% Zn–0.6at% Y. The mechanical properties of Mg–Y and Mg–Zn binary alloys were examined by some researchers using single crystals [28–31]. However, the effects of the coaddition of Zn and Y on the mechanical properties have not received significant attention until now. In this study, we used a single crystal prepared by directional solidification to ascertain the effects of coaddition. We found that the mechanical properties of the Mg solid solution are entirely different from those of pure Mg and similar to those of the LPSO phase, which we report here in detail. Moreover, the physical origin of the drastic increase in yield stress is discussed.

2. Experimental procedure

A master ingot with a composition of Mg–0.2at% Zn–0.6at% Y was prepared by induction melting in a carbon crucible. Directional solidification was conducted using the Bridgman technique (Nissin Giken NEV-DS2) in an Ar-gas atmosphere at a growth rate of 5.0 mm/h. The microstructure of the obtained DS crystal was examined by optical microscopy (OM; Olympus BX51M), laser microscopy (LM; Olympus DSX510), scanning electron microscopy (SEM; JEOL JSM-7800F) at 15 kV, and transmission electron microscopy (TEM; JEOL JEM-3010) at 300 kV. Furthermore, the distribution of Zn/Y atoms was examined by high-angle annular dark-field scanning transmission electron microscopy (HAADF-STEM; JEOL JEM-2100F) at 200 kV. In addition to the as-DS-grown crystals, the microstructure observation was conducted to some heat-treated specimens. As the first condition, some as-DS-grown specimens were annealed at 520°C for 5 h under Ar atmosphere, followed by water quenching. As the second condition, the specimen annealed at 520°C was further annealed at 400°C for 5 h, followed by water quenching. Then, the variations in microstructure in them were examined by abovementioned methods.

For comparison of the deformation behavior, pure-Mg single crystals were also grown by the same method at a growth rate of 10.0 mm/h. From the microstructural analyses, the obtained DS crystal was confirmed to consist of some large grains of the Mg solid solution phase with a diameter of ~ 5–8 mm. From the large grains, single-crystal rectangular specimens with dimensions of $2 \times 2 \times 5$ mm^3 were cut for compression tests by electrodischarge machining. The crystal orientation of the specimen was determined by X-ray backscatter Laue diffraction analysis.

Four different crystal orientations were selected as loading axes in the compression tests to examine the orientation dependence of the plastic deformation behavior. The four orientations correspond to [0001], [01$\bar{1}$0], [11$\bar{2}$0], and [1 1 $\bar{2}$ 1.85], as indicated in the stereographic projection in Fig. 2(a), later. The Schmid factors for the possible deformation modes for the four loading axes that were expected from reports on the deformation behavior of pure Mg and its solid solutions [28–38] are listed in Supplemental Tables S1 and S2. Before the compression tests, specimens were mechanically polished using emery paper and then chemically polished in an ethanol–20-vol% nitric acid solution to remove surface damage. Compression tests were performed at a nominal strain rate of 1.67×10^{-4} s^{-1} at temperatures ranging from RT (~20°C) to 400°C using universal testers (Shimadzu AG-5kNX System, and Instron 8862 System), in vacuum. The influence of the heat-treatment to the deformation behavior was also examined by the compression test using the abovementioned heat-treated specimens at [11$\bar{2}$0] at RT.

In addition, some tensile tests were conducted to examine the ductility of the as-DS-grown single crystal. The tensile tests were conducted by using the plate-like specimens with the gauge dimension of 2×1 mm^2 $\times$ 5 mm, along [0001] orientation at RT, in vacuum.

Deformation markings placed on specimen surfaces were analyzed using OM with Nomarski interference contrast, and the operative deformation mode was determined. The variation in the crystal orientation due to deformation was examined by electron backscatter diffraction (EBSD) pattern analysis in the SEM at a measured step distance of 1.0 μm. During the preparation of specimens for SEM-EBSD, a specimen's surface was mechanically polished using emery paper, and a final treatment was conducted using a cross-section polisher (JEOL IB19500CP). The deformation microstructure was further examined by TEM. Specimens for TEM observation were prepared by ion milling using Ar (Fishione Model 1051 TEM Mill,).

3. Results

3.1. Development of the LPSO nanoplate microstructure

Fig. 1(a) shows an SEM image of the microstructure of the as-grown DS $Mg_{99.2}Zn_{0.2}Y_{0.6}$ alloy. The DS alloy comprises some large Mg grains, and almost no large precipitates exist. In the grains, a very fine straight contrast exists along an alignment direction. From an X-ray Laue analysis, it was confirmed that fine traces exist parallel to the basal plane in the Mg grains. Fig. 1(b) shows a bright-field TEM image of the as-grown crystal viewed along [11$\bar{2}$0]. A large amount of stacking-fault-like contrast is seen on (0001). This is the origin of the fine traces from the SEM observations. The formation of stacking-fault-like defects in Mg–Zn–Y ternary alloys has been previously reported [39–41]. The TEM image shown in Fig. 1(b) was acquired with a reflection vector of $\mathbf{g}$ = 0002. The stacking faults on the basal plane in a general hexagonally close-packed (hcp) crystal have a shift vector of $\mathbf{R}$ = 1/3<10$\bar{1}$0>. Thus, the contrast of the stacking faults must be invisible if the existing stacking faults are conventional faults. The clear contrast of the defects in Fig. 1(b) demonstrates that they are not simple stacking faults but a thin LPSO-phase-related defect accompanied by the compositional segregation of Zn/Y atoms. The high-magnification TEM observations demonstrate that the fault-like contrast has a "thickness." The thickness of the fault-like contrast is approximately ~28 nm, and the number density of the fault-like contrast along the *c* axis is ~9.8 per 1 μm. We call this stacking-fault-like defect an "LPSO nanoplate" hereafter.

The detailed structure of the LPSO nanoplate was confirmed by HAADF-STEM, as shown in Fig. 1(c). The fault-like contrast is observed with white contrast owing to the segregation of Zn/Y atoms that are "heavier" than Mg, as reported previously [39–41]. The higher-magnification HAADF-STEM image in the inset of Fig. 1(c) demonstrates that the ordering of the Zn/Y segregation along the *c* axis has not developed to a long range but only along four atomic layers where an fcc-type stacking fault exists. This is consistent with the previous reports [40,41], which further detail their nature. In our Mg–Zn–Y single crystal, the four-layer Zn/Y segregated stacking faults are heterogeneously distributed, as some of them gather in a localized region, implying that the LPSO nanoplate is not a "perfect LPSO phase" but is composed of aggregated some four-layer Zn/Y segregated stacking faults. The thickness of the LPSO nanoplate measured by TEM is an "apparent thickness" corresponding to the average nanometer-scale distances of the aggre-

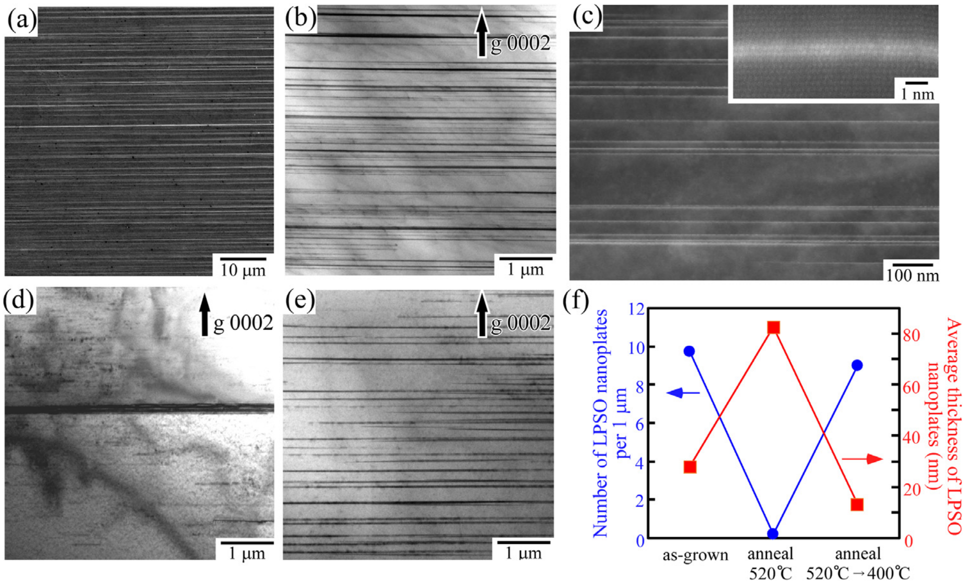

Fig. 1. (a) SEM image of the as-grown DS alloy. (b) Bright-field TEM image showing the microstructure in the as-grown alloy. (c) Corresponding HAADF-STEM image. The inset shows a higher-magnification image. Zn/Y atoms are segregated along four atomic layers where an fcc-type stacking fault exists. (d, e) TEM images showing the variation in microstructure due to heat treatment: (d) specimen in Fig. 1(b) was annealed at 520°C for 5 h followed by water quenching, and (e) specimen in Fig. 1(d) was annealed further at 400°C for 5 h. (f) Variation in the number of LPSO nanoplates per 1 μm and their average thickness according to heat treatment, measured along [0001] in the TEM. The observation direction is parallel to [11$\bar{2}$0] in all the Figs. 1(a–e).

gated Zn/Y segregated stacking faults. The schematics explaining the LPSO nanoplate is indicated in Supplementary Fig. S3.

Heat treatment was used to control the LPSO nanoplate microstructure. Fig. 1(d) shows the microstructure of a specimen annealed at 520°C for 5 h followed by water quenching, and Fig. 1(e) shows the variation in the microstructure after further annealing of this specimen at 400°C for 5 h. Fig. 1(f) shows the variations in the number density of LPSO nanoplates and their average thickness along the *c* axis according to heat treatment. The number of the LPSO nanoplates drastically decreases to below 0.1 /μm with high-temperature annealing at 520°C and is accompanied by an increase in the average thickness to ~ 83 nm. At high temperature of 520°C, Y and Zn are considered to show much higher solubility in Mg than those at low temperatures. At this condition, the LPSO nanoplate microstructure was thermally unstable. The volume fraction of the LPSO nanoplate was drastically decreased, and the small amount of remained LPSO nanoplates transformed into a perfect LPSO phase at a localized region. With subsequent annealing at 400°C, however, many thin LPSO nanoplates again precipitate, and the microstructure almost recovers to that of the as-grown crystal. These behaviors are similar to those of the Mg grains in a polycrystalline Mg–0.7at% Zn–1.4at% Y alloy, as reported by Lee et al. [39].

3.2. Drastic strengthening of Mg solid solution due to the LPSO nanoplates

Using the as-grown single crystal containing a high density of LPSO nanoplates, the mechanical properties were examined by compression tests. Fig. 2(a) shows the temperature dependence of the yield (fracture) stress in four loading orientations. The Schmid factors for the possible deformation modes for the four loading axes are listed in Supplemental Tables S1 and S2. The yield stress shows a strong dependence on orientation. Focusing on the yield stress at RT, the yield stress is extremely low: 9 MPa in the [1 1 $\bar{2}$ 1.85] orientation, and it slightly decreases to 7 MPa at 400°C. A high yield stress of >100 MPa was measured in the [01$\bar{1}$0] and [11$\bar{2}$0] orientations. The yield stress is slightly higher in the [11$\bar{2}$0] orientation than in the [01$\bar{1}$0] orientation, and it moderately decreases as the temperature increases in both orientations. An extremely high strength of >350 MPa was measured in the [0001] orientation, but all specimens were fractured before yielding.

In Fig. 2(a), the yield stresses of pure-Mg single crystals in ref. [32] and those measured in this study are plotted in gray for comparison. Surprisingly, the yield stress drastically varies, even with minute amounts of coadded 0.2at% Zn and 0.6at% Y. The yield stress in the [1 1 $\bar{2}$ 1.85] orientation is extremely low (~1 MPa) in pure-Mg single crystals, as expected from the previous report [30]. While the yield stress of the Mg–Zn–Y solid solution greatly increases relative to that of pure Mg. Furthermore, the yield stress in the [11$\bar{2}$0] orientation surprisingly increases from ~12 MPa to ~130 MPa, which is ~11 times larger for the Mg–Zn–Y solid solution, and retains plastic deformability. A similar drastic increase in the yield stress is observed in the [01$\bar{1}$0] orientation. In the [0001] orientation, the fracture stress of the Mg–Zn–Y solid solution is ~350 MPa, which 1.3 times larger than the yield stress of the pure-Mg single crystal. In contrast to the behavior of pure Mg, the high yield stress of the Mg–Zn–Y alloy is maintained even at high temperatures.

The typical stress-strain curves for deformation at RT and 300°C are displayed in Figs. 2(b) and (c). Except for the [0001] orientation, more than 5% plastic deformation is possible for all temperatures and loading orientations. Weak work hardening is observed for deformation in the [01$\bar{1}$0] orientation at RT, but almost no or a small amount of work hardening is observed after yielding under other loading conditions.

3.3. Deformation mechanisms of the Mg–Zn–Y alloy containing LPSO nanoplates

To clarify the origin of the strong orientation dependence of the deformation behavior of the single crystal of the Mg–Zn–Y solid solution, the deformation microstructure was examined. Fig. 3 shows OM images of the deformation traces introduced in specimens deformed at RT to ~5% plastic strain. In the [1 1 $\bar{2}$ 1.85] orientation, a large number of fine slip traces are observed [Figs. 3(a, b)]. These slip traces are introduced parallel to the LPSO nanoplates

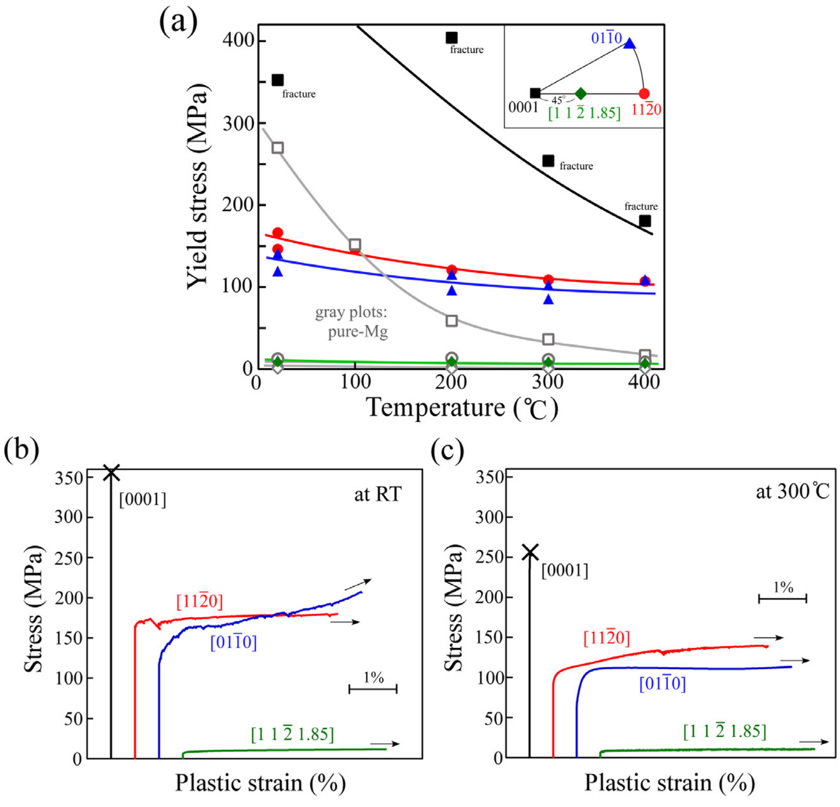

Fig. 2. (a) Temperature dependence of the yield stress of the as-grown $Mg_{99.2}Zn_{0.2}Y_{0.6}$ single crystal in four loading orientations. The yield stress of the pure-Mg single crystals reported in ref. [32] and that measured in this study are also plotted in gray for comparison. (b, c) Typical stress–strain curves deformed at (b) RT and (c) 300°C in four different loading orientations.

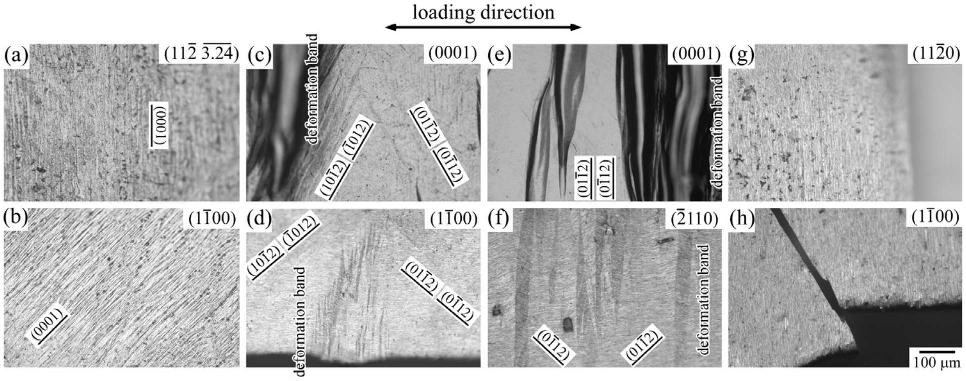

Fig. 3. OM images showing the deformation traces in specimens deformed at RT. Specimens were deformed to ~5% plastic strain in the loading orientations of (a, b) [1 1 $\bar{2}$ 1.85], (c, d) [$11\bar{2}0$], (e, f) [$01\bar{1}0$], and (g, h) [0001]. The Miller indices of the side surface planes in observation are indicated at the top-right corner in the images.

shown in Fig. 1(a), demonstrating that the slip plane is parallel to (0001). From a TEM analysis, the Burgers vector of a basal dislocation was confirmed to be <$11\bar{2}0$>, the same as that in pure Mg. A nearly similar morphology of (0001) basal slip traces was observed at any temperature. In the [0001] orientation, specimens fractured at a very high stress of ~350 MPa before yielding. In the fractured specimens, no deformation traces are observed [Figs. 3(g, h)]. Even at high temperature, no large plastic strain is obtained, and the introduction of deformation traces is not observed, as indicated in Supplemental Fig. S4. Thus, the deformation mechanism in the [0001] orientation is still unknown. Figs. 3(c, d) show the deformation markings introduced in the specimen deformed in the [$11\bar{2}0$] orientation. Broad deformation bands whose interfaces are parallel to {$10\bar{1}2$} are abundantly observed. According to results reported for pure Mg [33], the deformation bands are considered to be {$10\bar{1}2$} deformation twins. In addition to {$10\bar{1}2$} twins, some deformation bands whose traces are wavy and introduced nearly perpendicular to the loading axis coexist. The contrast of these wavy deformation bands is strong on the (0001) side surface [Fig. 3(c)], but weak on the ($1\bar{1}00$) side surface [Fig. 3(d)]. The formation of such wavy deformation bands is more readily observed for the specimen deformed in the [$01\bar{1}0$] orientation [Figs. 3(e, f)]. The contrast of the wavy deformation bands has similar features as that for the specimen deformed in the [$11\bar{2}0$] orientation; the contrast of the deformation bands is much stronger on the (0001) side surface.

Figs. 4(a, b) show macroscopic views of the variations in the deformation microstructure with temperature, for specimens deformed in the [$11\bar{2}0$] and [$01\bar{1}0$] orientations, respectively. In contrast to the results for specimens deformed in the [1 1 $\bar{2}$ 1.85] and

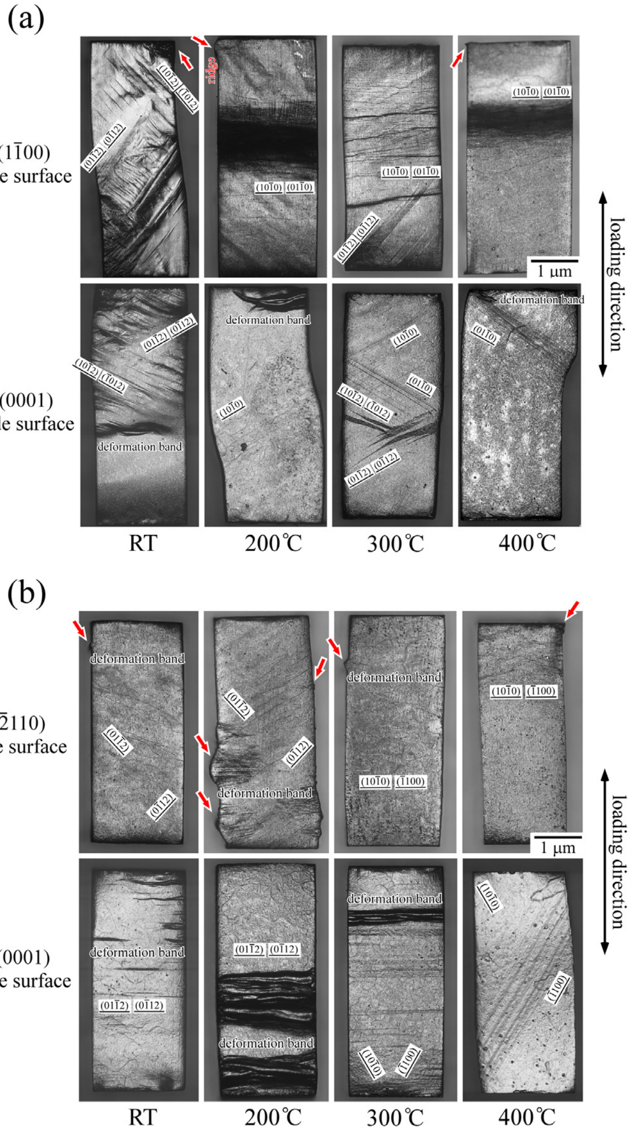

Fig. 4. Macroscopic views showing the variations in the deformation microstructure with temperature. Specimens were deformed in the (a) $[11\bar{2}0]$ and (b) $[01\bar{1}0]$ loading orientations to ~5% plastic strain at the temperatures indicated. The Miller indices of the side surface planes in observation are indicated in the figure.

[0001] orientations, the operative deformation mode varies with temperature. For deformation along $[11\bar{2}0]$ at RT, the formation of $\{10\bar{1}2\}$ twins is predominant, and a small number of wavy deformation bands locally coexist. Significant “ridge” formation is confirmed when observed on the $(1\bar{1}00)$ side surface by the formation of wavy deformation bands, as indicated by red arrows; however, the side surface remains straight, even after the formation of deformation bands when observed on (0001) side surface. This indicates that the macroscopic shear direction of the wavy deformation bands is parallel to [0001]. This is the origin of the much stronger contrast of the wavy deformation bands on the (0001) side surface in Fig. 3(c). A similar deformation microstructure is observed at 100°C. However, at and above 200°C, the formation of $\{10\bar{1}2\}$ twins drastically decreases; instead, fine slip traces are introduced in addition to the wavy deformation bands. A two-face trace analysis demonstrates that the slip trace is derived from $\{10\bar{1}0\}$ prismatic slip. The feature of the contrast of the slip traces; they are faint on (0001) but strong on $(1\bar{1}00)$ side surface, suggesting that the operative slip system is $\{10\bar{1}0\}<1\bar{2}10>$. This was further confirmed by a TEM **g•b** dislocation contrast analysis. Note that the slip traces of the $\{10\bar{1}0\}$ prismatic slip become wavy when observed on the $(1\bar{1}00)$ side surface at high temperatures, although they are relatively straight at 200°C. This indicates that cross-slip events frequently occur in the $\{10\bar{1}0\}$ prismatic slip at and above 300°C with the help of thermal activation.

In the $[01\bar{1}0]$ loading orientation, the formation of wavy deformation bands is the predominant deformation mode from RT up to 300°C. The formation of a ridge on a side surface is apparent when observed on $(\bar{2}110)$ but not on (0001), as indicated by the arrows. The variations in the shapes of the specimens in Figs. 4(a, b) demonstrate that the shear direction for the formation of wavy deformation bands is always parallel to [0001], irrespective of loading orientation. A small number of $\{10\bar{1}2\}$ twins coexist between wavy deformation bands, but their contrast is weak. At and above 300°C, $\{10\bar{1}0\}$ prismatic slip occurs in addition to the formation of wavy deformation bands, similar to that observed in the $[11\bar{2}0]$ loading orientation.

To clarify the nature of the wavy deformation bands, SEM-EBSD analysis was conducted for the specimen deformed in the $[11\bar{2}0]$ orientation at RT. Figs. 5(a, b) show the typical crystal orientation maps for (a) $\{10\bar{1}2\}$ twins and (b) wavy deformation bands. Corresponding to the crystal orientation maps, Figs. 5(c, d) show the distributions of the crystal rotation angle with respect to the matrix (undeformed region) in the deformation bands. This rotation angle is defined in Fig. 5(h). Additionally, the crystal rotation axis in the measured band is indicated by color in the bar graphs; green means near $<\bar{2}110>$, and blue means near $<1\bar{1}00>$ with a deviation-angle tolerance of 10°. In the region shown in Fig. 5(a), the crystal rotation angle is in the range of 80°–90° in all deformation bands, and the crystal rotation axis is along $<\bar{2}110>$. This is in agreement with the crystallographic features of $\{01\bar{1}2\}$ twins; the ideal crystal rotation angle is 86° along $<\bar{2}110>$ [36]. In contrast, the crystal rotation angle in the region shown in Fig. 5(b) has a wide distribution ranging from ~5° to ~55°, although the crystal rotation axis is almost completely parallel to $<1\bar{1}00>$. This is different from that observed for deformation twins, in which the crystal rotation angle is fixed because they possess a definite crystal orientation relationship with respect to the matrix. This indicates that the formed wavy deformation bands are not twins but deformation kink bands, as observed in the LPSO phase [42]. The change in the crystal rotation angle is induced by the variation in the number of basal dislocations that form the kink band boundary [21,42–46].

Fig. 5(e) shows the crystal orientation map for the specimen deformed in the $[01\bar{1}0]$ orientation at RT. There is almost no change in color of the crystal orientation, demonstrating that crystal rotation in the deformation band occurs along a rotation axis parallel to the observed $[\bar{2}110]$ surface normal. Fig. 5(f) shows the crystal orientation map for the same region, but the colors in the map indicate a crystal orientation along the loading axis. Fig. 5(g) shows the corresponding distribution of the crystal rotation angle in the band. The distribution of the rotation angle shows two obvious peaks—a broad peak around 25° and a sharp peak around 85°. The former and latter correspond to a deformation kink band and $\{01\bar{1}2\}$ twin, respectively. In Fig. 5(f), the kink bands and $\{01\bar{1}2\}$ twins are shown purple and red, respectively. Kink bands and $\{01\bar{1}2\}$ twins collectively form during deformation in the $[01\bar{1}0]$ orientation. This may be related to the appearance of weak work hardening during deformation, as shown in Fig. 2(b). In Fig. 5(f), there is almost no difference in the red color of the $\{01\bar{1}2\}$ twin at all locations, but the purple color of the deformation kink band changes with location. This is evidence that the crystal rotation angle is not fixed in the deformation kink bands.

The rotation axes of the kink bands are different in Figs. 5(b) and (e): $<1\bar{1}00>$ and $<\bar{2}110>$, respectively. This implies that the rotation axis varies such that it is perpendicular to the loading ori-

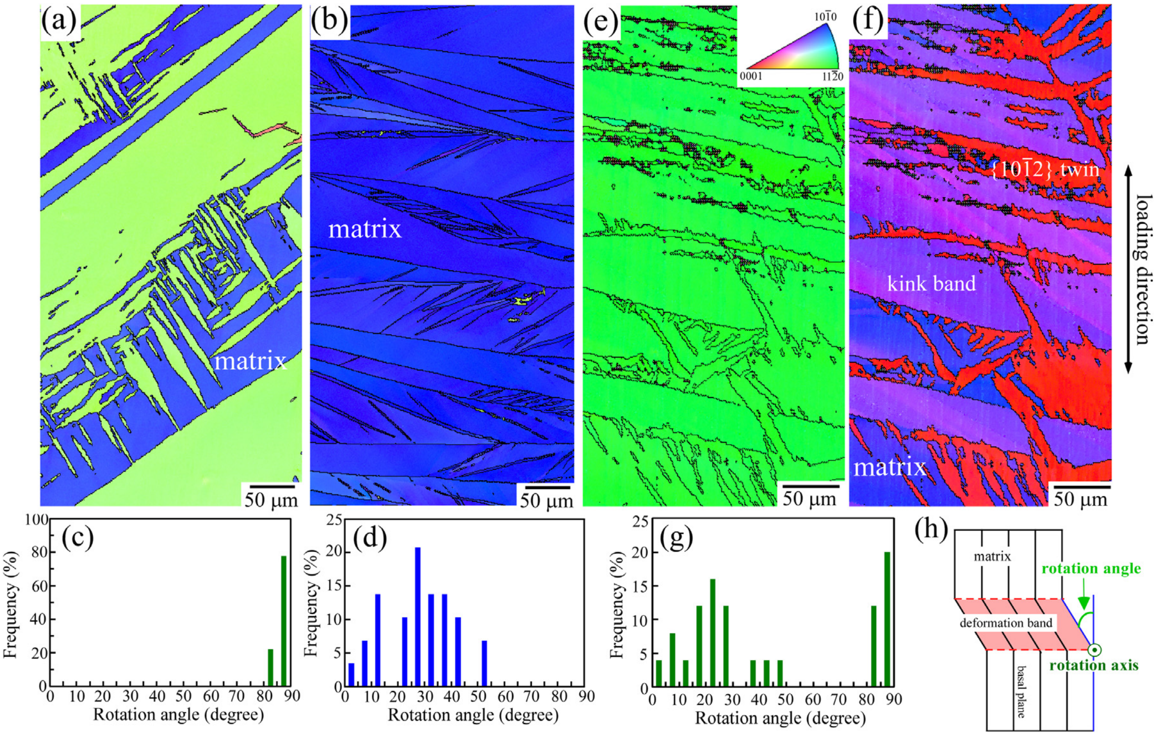

Fig. 5. (a, b) Crystal orientation maps of deformation microstructures of the specimen deformed in the $[11\bar{2}0]$ orientation at RT to ~5% plastic strain and observed on the $(1\bar{1}00)$ side surface. (c, d) Distributions of the crystal rotation angle in the deformation bands with respect to the matrix (undeformed region), measured in the regions around Fig. 5(a) and (b), respectively. (e) Crystal orientation map of the specimen deformed in the $[01\bar{1}0]$ orientation at RT to ~5% plastic strain and observed on the $(\bar{2}110)$ side surface. (f) The same region in Fig. 5(e), but the colors in the map indicate the crystal orientation along the loading axis, in order to distinguish the orientation colors of the deformation twins and deformation kink bands. (g) Distribution of the crystal rotation angle in the region around Fig. 5(e). The colors of the bar graph of Figs. 5(c), (d), and (g) indicate the crystal rotation axis of the measured bands: green: near $<\bar{2}110>$ and blue: near $<1\bar{1}00>$ with a deviation-angle tolerance of 10°. (h) Schematic showing the definitions of the crystal rotation angle and crystal rotation axis in the deformation band.

entation on the [0001] zone axis. This arbitrariness of the crystal rotation angle and axis in the deformation kink bands demonstrates that the boundary of a kink band comprises the alignment of basal dislocations along a direction perpendicular to their slip plane, as observed in the LPSO phase and illustrated in Supplementary Fig. S2. The change in the crystal rotation axis is induced by the variation in the type of Burgers vector of the basal dislocations that form the kink band [21,42–46]. The observed unique features of the deformation bands—the change in crystal rotation axis in the band with loading orientation and the wavy morphology of the band observed on (0001) side surface—are in good agreement with previous reports on deformation kink bands in a Zn single crystal [44] and the LPSO phase [42,45].

Fig. 6(a) shows a bright-field TEM image of deformation kink bands, several of which locally accumulate. In the image, the trace of the basal plane is indicated by the green line. Significant crystal rotation with nonfixed angle can be recognized. Fig. 6(b) shows a higher-magnification image of the kink bands, and Figs. 6(c–f) show selected-area electron diffraction (SAED) patterns at points A–D in Fig. 6(b). The SAED pattern at point B almost corresponds to a $<1\bar{1}00>$ net SAED pattern. From the SAED patterns at points A, C, and D, the crystal is largely rotated almost along the $[1\bar{1}00]$ observation direction by the formation of kink bands, as measured in the SEM-EBSD analysis [Fig. 5(b)]. The directions of the *c* axis measured from SAED patterns are indicated in Fig. 6(b) for each kink band. Here, the rotation angle almost directly corresponds to the bending angle of the LPSO nanoplates. This demonstrates that the change in the crystal orientation does not occur by the shuffling of atomic positions, which occurs during the formation of a deformation twin in the hcp materials. Instead, this change occurs by the direct shear movement of atoms. In addition to the high-

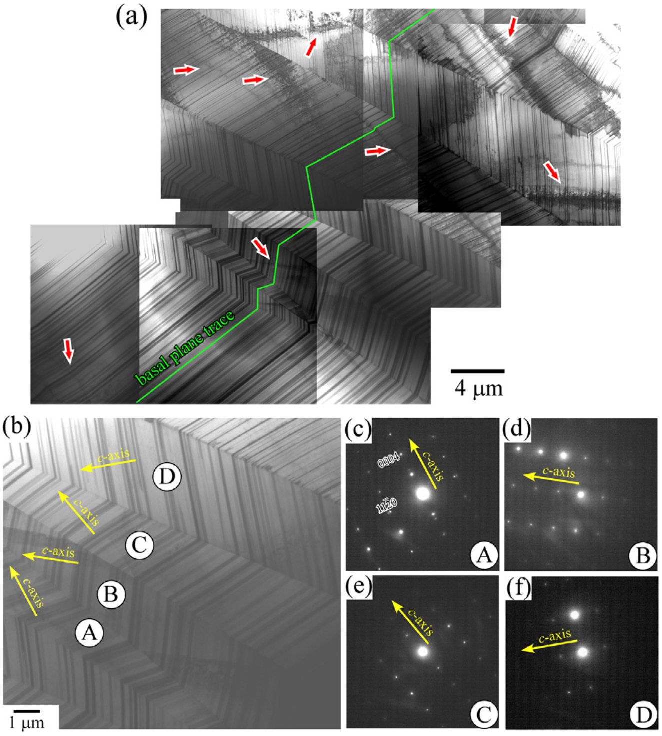

Fig. 6. (a) Bright-field TEM image of the deformation kink bands introduced in the specimen deformed in the $[11\bar{2}0]$ orientation at RT to ~5% plastic strain. The observation direction is nearly parallel to $[1\bar{1}00]$ in the matrix. (b) Higher-magnification image of the kink bands. (c–f) SAED patterns taken at points A–D indicated in Fig. 6(b).

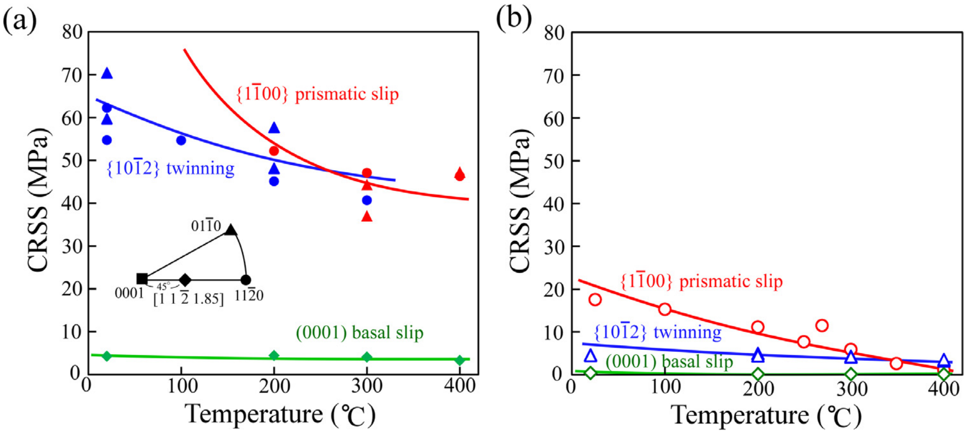

Fig. 7. (a) Temperature dependencies of the CRSS estimated in the as-grown $Mg_{99.2}Zn_{0.2}Y_{0.6}$ single crystal investigated in this study, and (b) those in pure-Mg single crystals reported in refs. [33–35] and measured in this study.

angle kink-band boundaries, many low-angle boundaries with a rotation angle of less than 15° coexist, as indicated by the red arrows in Fig. 6(a). Note that the morphology of the kink bands is very similar to that of the deformed LPSO phase [18–20].

4. Discussion

4.1. Strengthening mechanism due to the LPSO nanoplates

We observed a drastic increase in the yield stress even with the coaddition of minute amounts of Zn and Y. The formation of LPSO nanoplates is strongly suggested to be the origin of this increase in yield stress. Fig. 7(a) shows the temperature dependence of the critical resolved shear stress (CRSS) for the operative deformation modes in a single crystal of the Mg–Zn–Y solid solution, as estimated from the results in Figs. 2–5. The CRSS for a deformation kink band cannot be defined because its elementary formation process is still unclear. Thus, it is not shown in this graph. For comparison, the CRSSs of pure-Mg single crystals reported in refs. [33–35] and those measured in this study are plotted in Fig. 7(b).

These results demonstrate that the existence of LPSO nanoplates drastically increases the CRSSs for {10$\bar{1}$2} twins and {10$\bar{1}$0} prismatic slip since their operation must intersect with LPSO nanoplates. For the compression of pure Mg in the [0001] orientation, the operation of several twinning systems such as {10$\bar{1}$1} twins and {11$\bar{2}$2}<11$\bar{2}\bar{3}$> pyramidal slip is reported in refs. [34,37]. However, they were not observed in the Mg–Zn–Y solid solution, which has a much higher fracture stress in the [0001] loading orientation. This implies that not only the CRSSs for twinning systems but that for {11$\bar{2}$2}<11$\bar{2}\bar{3}$> slip are also drastically increased owing to the intersection with LPSO nanoplates.

To clarify the effects of the LPSO nanoplates more quantitatively, Fig. 8(a) shows the variation in the yield stress in the [11$\bar{2}$0] orientation at RT with heat treatment. The yield stress decreases with annealing at 520°C owing to the reduction in the density of LPSO nanoplates, as shown in Fig. 1(d). However, the high yield stress is almost recovered with further annealing at 400°C, which is derived from the reprecipitation of LPSO nanoplates, as shown in Fig. 1(e). Fig. 8(b, c) show the corresponding deformation microstructures of the specimens. As expected, the formation of deformation twins is observed for the specimen annealed at 520°C owing to the reduction in the number of LPSO nanoplates. While kink-band formation is again observed for the specimen annealed at 400°C and accompanied by an increase in the yield stress. These results obviously demonstrate that the LPSO nanoplates prohibit the formation of {10$\bar{1}$2} deformation twins, and the formation of deformation kink bands is induced as the alternative accommodation process of plastic deformation.

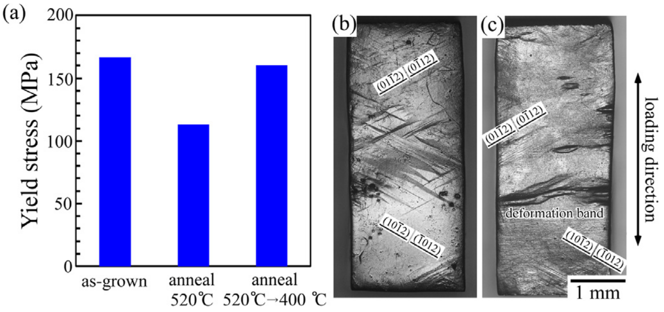

Fig. 8. (a) Variation in the yield stress with heat treatment for deformation in the [11$\bar{2}$0] orientation at RT. (b, c) Macroscopic views of the deformation microstructure in specimens (b) annealed at 520°C for 5 h, and (c) annealed further at 400°C for 5 h, prior to compression tests. The side surface planes in observation are parallel to (0001).

The CRSS for basal slip is also increased relative to that for pure Mg. However, it is comparable or moderately smaller than that measured for a Mg–Y binary single crystal [28], implying that the increase in the CRSS of the single crystal of the Mg–Zn–Y solid solution is almost induced by solid-solution hardening by Y/Zn atoms, and the additional effect of the development of LPSO nanoplates is small since they exist parallel to the (0001) slip plane.

4.2. Comparison of the yield stress to that of the bulk LPSO phase alloy

Fig. 9 shows a comparison of the yield stresses of a single crystal of the Mg–Zn–Y solid solution and the bulk LPSO-single-phase DS crystal [20] with a composition of $Mg_{85}Zn_6Y_9$. In both crystals, the formation of kink bands is observed when the macroscopic operation of basal slip is hindered. More precisely, kink bands are observed for the compressive deformation of the Mg–Zn–Y single crystal in the [01$\bar{1}$0] and [11$\bar{2}$0] orientations, and of the LPSO-phase DS crystal loaded parallel to the growth direction (0° direction), where the basal plane is parallel to the loading orientation. Surprisingly, the yield stresses show similar high values for both alloys when kink-band formation occurs. This obviously demonstrates that even in a dilute Mg–Zn–Y alloy that does not contain the "perfect" LPSO phase, the precipitation of LPSO nanoplates effectively induces the formation of deformation kink bands by pre-

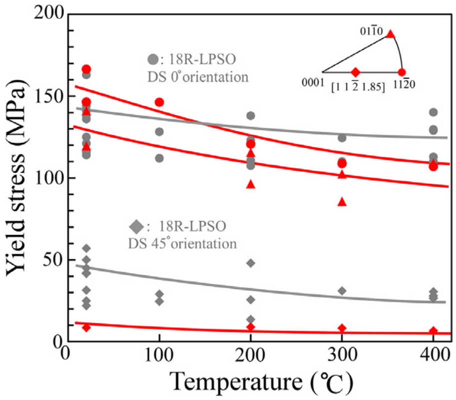

Fig. 9. Comparison of yield stresses of the as-grown $Mg_{99.2}Zn_{0.2}Y_{0.6}$ single crystal and LPSO phase. The yield stresses of the $Mg_{99.2}Zn_{0.2}Y_{0.6}$ single crystal are indicated by the red points. In addition, the DS 18R-LPSO phase previously reported in ref. [20] are indicated by the gray points.

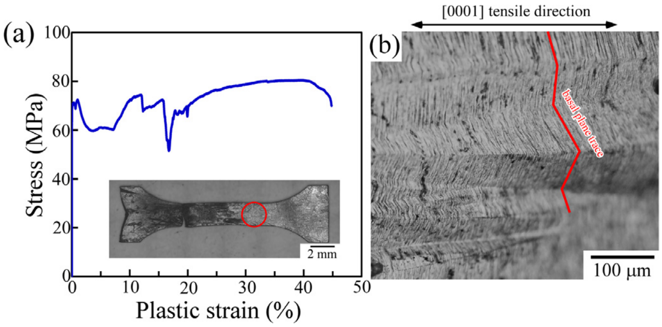

Fig. 10. (a) Stress-strain curve in the tensile test of $Mg_{99.2}Zn_{0.2}Y_{0.6}$ single crystal along [0001] at RT. The entire view of the deformed specimen is inserted in the figure. (b) Higher magnification image of the deformation microstructure showing the formation of many deformation kink bands, observed at the part indicated by the red circle in Fig. 10(a). The side surface planes in observation is parallel to (10$\bar{1}$0).

venting the operation of other deformation modes except basal slip.

The yield stress of the LPSO phase in the 45° orientation—in which basal slip is operative—is moderately higher than that of $Mg_{99.2}Zn_{0.2}Y_{0.6}$ in the [1 1 $\bar{2}$ 1.85] orientation. This is derived from the polycrystalline microstructure of the DS LPSO-phase alloy. Indeed, Inoue et al. estimated the CRSS for basal slip in an LPSO-phase single crystal to be ~7 MPa using a micropillar compression test [47]. This is comparable to that of $Mg_{99.2}Zn_{0.2}Y_{0.6}$ in this study [Fig. 7(a)].

The biggest difference of the mechanical property between them is the tensile deformability by kink-band formation. Fig. 10(a) show the tensile deformation behavior of $Mg_{99.2}Zn_{0.2}Y_{0.6}$ single crystal along [0001] at RT. In pure-Mg single crystal, the tensile yield stress along [0001] showed a low value of ~5 MPa by the formation of {10$\bar{1}$2} twin. However, much higher yield stress of ~55 MPa was obtained in the $Mg_{99.2}Zn_{0.2}Y_{0.6}$ single crystal, accompanied by the formation of kink-bands as shown in Fig. 10(b). This is because the formation of kink-band generates the tensile strain along [0001], as schematically indicated in supplementary Fig. S2. More higher yield stress is ideally expected from the result shown in Fig. 2(a), but local deformation by basal slip occurred at the hooked part of the tensile specimen prior to the kink-bands formation at the gauge section, owing to the strong plastic anisotropy. As far as the authors know, this is the first report directly demonstrating the tensile ductility by kink-band formation in a bulk material. In the LPSO phase DS alloy, large tensile ductility by kink-band formation has not been confirmed until now, since grain boundary fracture frequently occurs before the formation of kink bands. This indicates the superiority of $Mg_{99.2}Zn_{0.2}Y_{0.6}$ alloy in terms of ductility without the decrease in strength compared to the LPSO phase alloy.

4.3. Possibility of the development of novel high-strength Mg alloys using LPSO nanoplates, beyond the "stacking-fault" strengthening

Until now, it was believed that the excellent mechanical properties of a Mg/LPSO two-phase alloy are induced by the LPSO phase as a strengthening phase. However, the present results indicate that changes in the mechanical properties of the Mg matrix phase may also strongly contribute to these excellent mechanical properties when the Mg matrix phase contains LPSO nanoplates. The results suggest that the strengthening mechanism of the Mg/LPSO two-phase alloy must be reconsidered depending on the microstructure.

Furthermore, the obtained results strongly suggest that there is a significant possibility that an ultrahigh-strength lightweight alloy based on a dilute Mg–Zn–Y alloy—comparable or superior than those of the Mg/LPSO two-phase alloys—is expected to be developed via the appropriate control of LPSO nanoplate microstructures. Since Y is an expensive rare metal, the requirement of a large amount of Y is a major drawback for broadening the practical application of Mg/LPSO two-phase alloys. The present findings enable the development of novel affordable high-strength Mg alloys.

Several studies report the strengthening of metallic materials by the introduction of large numbers of stacking faults and/or thin planar faults in Mg [48,49], Al [50], Ti [51], Co [52], CoCr [53], etc. In this study, this stacking-fault strengthening is more significantly enhanced using the unique features of the Mg–Zn–Y alloy, as the coadded Y and Zn atoms preferentially segregate at stacking faults [39–41] to form LPSO nanoplates. We call this "mille-feuille microstructural control," in which a soft (Mg layer) and hard (Zn/Y segregated layer) layers are alternately stacked [54,55]. The results demonstrate that mille-feuille microstructural control induces the formation of deformation kink bands, imparting greater ductility and strength.

The present results only focus on the mechanical properties of a single crystal without macroscopic microstructural control. Nevertheless, the yield stress was surprisingly increased compared to that of pure Mg. It is known that the yield stress of the LPSO-phase alloy is drastically increased by grain refinement due to the increase in the formation stress of kink bands [27]. Thus, microstructural control of the dilute Mg–Zn–Y alloy has significant potential to enable an additional drastic increase in strength. This has been carried out by our group; the results will be published elsewhere.

5. Conclusion

(1) In the $Mg_{99.2}Zn_{0.2}Y_{0.6}$ single crystal grown by Bridgeman method, significant amount of stacking-fault-like platelet defects, called LPSO nanoplate, are formed parallel to the basal plane.
(2) The yield stress of $Mg_{99.2}Zn_{0.2}Y_{0.6}$ anomalously increases compared to that of pure Mg in many loading orientations where basal slip is not operative, owing to the presence of LPSO nanoplates. Surprisingly, the yield stress shows nearly the same value as that of the LPSO-single-phase alloy.
(3) The formation of deformation twins is strongly prohibited in the $Mg_{99.2}Zn_{0.2}Y_{0.6}$ single crystal by the LPSO nanoplates. Instead, the formation of deformation kink bands carries the strain, resulting in a high yield stress accompanied by large ductility.

(4) “LPSO nanoplate strengthening” has a high potential for developing new ultrahigh-strength Mg alloys with much lower Zn and Y contents.

Declaration of Competing Interest

The authors declare that they have no known competing financial interests or personal relationships that could have appeared to influence the work reported in this paper.

Acknowledgements

This work was supported by the Japan Society for the Promotion of Science (JSPS) KAKENHI for Scientific Research in Innovative Areas: “MFS Materials Science” (grant numbers JP18H05478, JP18H05476, and JP18H05475) and partly supported by JSPS KAKENHI JP18H05254. This work was also supported by JST, CREST (grant number JPMJCR2094), Japan.

Supplementary materials

Supplementary material associated with this article can be found, in the online version, at doi:10.1016/j.actamat.2021.116797.

References

[1] F. Pan, M. Yang, X. Chen, A Review on casting magnesium alloys modification of commercial alloys and development of new alloys, J. Mater. Sci. Tec. 32 (2016) 1211–1221.
[2] Y. Kawamura, K. Hayashi, A. Inoue, T. Masumoto, Rapidly solidified powder metallurgy Mg97Zn1Y2 alloys with excellent tensile yield strength above 600 MPa, Mater. Trans. 42 (2001) 1172–1176.
[3] K. Hagihara, A. Kinoshita, Y. Sugino, M. Yamasaki, Y. Kawamura, H.Y. Yasuda, Y. Umakoshi, Effect of long-period stacking ordered phase on mechanical properties of Mg97Zn1Y2 extruded alloy, Acta Mater 58 (2010) 6282–6293.
[4] K. Hagihara, A. Kinoshita, Y. Sugino, M. Yamasaki, Y. Kawamura, H.Y. Yasuda, Y. Umakoshi, Plastic deformation behavior of Mg89Zn4Y7 extruded alloy composed of long-period stacking ordered phase, Intermetallics 18 (2010) 1079–1085.
[5] M. Yamasaki, K. Hashimoto, K. Hagihara, Y. Kawamura, Effect of multimodal microstructure evolution on mechanical properties of Mg–Zn–Y extruded alloy, Acta Mater 59 (2011) 3646–3658.
[6] E. Oñorbe, G. Garcés, P. Pérez, P. Adeva, Effect of the LPSO volume fraction on the microstructure and mechanical properties of Mg–Y_{2X}–Zn_X alloys, J. Mater. Sci. 47 (2012) 1085–1093.
[7] J. Wang, P. Song, X. Zhou, X. Huang, F. Pan, Influence of the morphology of long-period stacking ordered phase on the mechanical properties of as-extruded Mg–5Zn–5Y–0.6Zr magnesium alloy, Mater. Sci. Eng. A 556 (2012) 68–75.
[8] K. Hagihara, A. Kinoshita, Y. Fukusumi, M. Yamasaki, Y. Kawamura, High-temperature compressive deformation behavior of Mg97Zn1Y2 extruded alloy containing a long-period stacking ordered (LPSO) phase, Mater. Sci. Eng. A 560 (2013) 71–79.
[9] E. Oñorbe, G. Garcés, F. Dobes, P. Pérez, P. Adeva, High-temperature mechanical behavior of extruded Mg-Y-Zn alloy containing LPSO phases, Metall. Mater. Trans. A 44 (2013) 2869–2883.
[10] L.B. Tong, X.H. Li, H.J. Zhang, Effect of long period stacking ordered phase on the microstructure, texture and mechanical properties of extruded Mg–Y–Zn alloy, Mater. Sci. Eng. A 563 (2013) 177–183.
[11] G. Garces, P. Perez, S. Cabeza, H.K. Lin, S. Kim, W. Gan, P. Adeva, Reverse tension/compression asymmetry of a Mg-Y-Zn alloys containing LPSO phases, Mater. Sci. Eng. A 647 (2015) 287–293.
[12] J.K. Kim, S. Sandlöbes, D. Raabe, On the room temperature deformation mechanisms of a Mg-Y-Zn alloy with long-period-stacking-ordered structures, Acta Mater 82 (2015) 414–423.
[13] H. Liu, J. Bai, K. Yan, J. Yan, A. Ma, J. Jiang, Comparative studies on evolution behaviors of 14H LPSO precipitates in as-cast and as-extruded Mg-Y-Zn alloys during annealing at 773 K, Mater. Design 93 (2016) 9–18.
[14] R. Chen, S. Sandlöbes, X. Zeng, D. Li, S. Korte-Kerzel, D. Raabe, Room temperature deformation of LPSO structures by non-basal slip, Mater. Sci. Eng. A 682 (2017) 354–358.
[15] G. Garcés, K. Máthis, J. Medina, K. Horváth, D. Drozdenko, E. Oñorbe, P. Dobroň, P. Pérez, M. Klaus, P. Adeva, Combination of in-situ diffraction experiments and acoustic emission testing to understand the compression behavior of Mg-Y-Zn alloys containing LPSO phase under different loading conditions, Inter. Jour. Plast. 106 (2018) 107–128.
[16] D. Egusa, E. Abe, The structure of long period stacking/order Mg–Zn–RE phases with extended non-stoichiometry ranges, Acta Mater 60 (2012) 166–178.
[17] E. Abe, A. Ono, T. Itoi, M. Yamasaki, Y. Kawamura, Polytypes of long-period stacking structures synchronized with chemical order in a dilute Mg–Zn–Y alloy, Philo. Mag. Lett. 91 (2011) 690–696.
[18] K. Hagihara, N. Yokotani, Y. Umakoshi, Plastic deformation behavior of $Mg_{12}YZn$ with 18R long-period stacking ordered structure, Intermetallics 18 (2010) 267–276.
[19] K. Hagihara, Y. Sugino, Y. Fukusumi, Y. Umakoshi, T. Nakano, Plastic deformation behavior of $Mg_{12}ZnY$ LPSO-phase with 14H-typed structure, Mater. Trans. 52 (2011) 1096–1103.
[20] K. Hagihara, T. Okamoto, H. Izuno, M. Yamasaki, M. Matsushita, T. Nakano, Y. Kawamura, Plastic deformation behavior of 10H-type synchronized LPSO phase in a Mg-Zn-Y system, Acta Mater 109 (2016) 90–102.
[21] J.B Hess, C.S. Barrett, Structure and nature of kink bands in zinc, Trans. Am. Inst. Min. Met. Eng. 185 (1949) 599–606.
[22] M.W. Barsoum, T. El-Raghy, Room temperature ductile carbides, Metall. Mater. Trans. A 30A (1999) 363–369.
[23] M.W. Barsoum, T. Zhen, A. Zhou, S. Basu, S.R. Kalidindi, Microscale modeling of kinking nonlinear elastic solids, Phys. Rev. B 71 (2005) 134101.
[24] T. Zhen, M.W. Barsoum, S.R. Kalidindi, Effects of temperature, strain rate and grain size on the compressive properties of Ti_3SiC_2, Acta Mater 53 (2005) 4163–4171.
[25] A.G. Zhou, M.W. Barsoum, Kinking nonlinear elastic deformation of Ti_3AlC_2, Ti_2AlC, $Ti_3Al(C_{0.5},N_{0.5})_2$ and $Ti_2Al(C_{0.5},N_{0.5})$, J. Alloys Comp. 498 (2010) 62–70.
[26] K. Hagihara, Z. Li, M. Yamasaki, Y. Kawamura, T. Nakano, Strengthening mechanisms acting in extruded Mg-based long-period stacking ordered (LPSO)-phase alloys, Acta Mater 15 (2019) 226–239.
[27] K. Hagihara, M. Yamasaki, Y. Kawamura, T. Nakano, Strengthening of Mg-based long-period stacking ordered (LPSO) phase with deformation kink bands, Mater. Sci. Eng. A 763 (2019) 138163.
[28] S. Miura, S. Imagawa, T. Toyoda, K. Ohkubo, T. Mohri, Effect of rare-earth elements Y and Dy on the deformation behavior of Mg alloy single crystals, Mater. Trans. 49 (2008) 952–956.
[29] H. Rikihisa, T. Mori, M. Tsushida, H. Kitahara, S. Ando, Influence of yttrium addition on plastic deformation of magnesium, Mater. Trans. 58 (2017) 1656–1663.
[30] A. Akhtar, E. Teghtsoonian, Solid solution strengthening of magnesium single crystals-I alloying behaviour in basal slip, Acta Metall 17 (1969) 1339–1349.
[31] A. Akhtar, E. Teghtsoonian, Solid solution strengthening of magnesium single crystals-II the effect of solute on the ease of prismatic slip, Acta Metall 17 (1969) 1351–1356.
[32] H. Yoshinaga, R. Horiuchi, Deformation mechanisms in magnesium single crystals compressed in the direction parallel to hexagonal axis, Trans JIM 4 (1963) 1–8.
[33] A. Chapuis, J.H. Driver, Temperature dependency of slip and twinning in plane strain compressed magnesium single crystals, Acta Mater 59 (2011) 1986–1994.
[34] H. Yoshinaga, R. Horiuchi, On the nonbasal slip in magnesium crystals, Trans JIM 5 (1964) 14–21.
[35] B.C. Wonsiewicz, W.A. Backofen, Plasticity of magnesium crystals, Trans. Metall. Soc. AIME 239 (1967) 1422–1431.
[36] N. Stanford, Observation of {1121} twinning in a Mg-based alloy, Philo. Mag. Lett. 88 (2008) 379–386.
[37] T. Obara, H. Yoshinaga, S. Morozumi, {1122}<1123>slip system in magnesium, Acta Metall. 21 (1973) 845–853.
[38] M.H. Yoo, Slip, twinning, and fracture in hexagonal close-packed metals, Metall. Trans. A 12 (1981) 409–418.
[39] J. Lee, K. Sato, T.J. Konno, K. Hiraga, Stabilization of stacking faults and a long period stacking phase dispersed in α-Mg crystalline grains of Mg-0.7 at%Zn-1.4 at%Y alloy, Mater. Trans. 50 (2009) 222–225.
[40] Y.M. Zhu, A.J. Morton, M. Weyland, J.F. Nie, Characterization of planar features in Mg–Y–Zn alloys, Acta Mater 58 (2010) 464–475.
[41] J.-K. Kim, W.-S. Ko, S. Sandlobes, M. Heidelmann, B. Grabowski, D. Raabe, The role of metastable LPSO building block clusters in phase transformations of an Mg-Y-Zn alloy, Acta Mater 112 (2016) 171–183.
[42] K. Hagihara, M. Yamasaki, M. Honnami, H. Izuno, M. Tane, T. Nakano, Y. Kawamura, Crystallographic nature of deformation bands shown in Zn and Mg-based long period stacking ordered (LPSO) phase, Philo. Mag. 95 (2015) 132–157.
[43] M. Yamasaki, K. Hagihara, S. Inoue, J.P. Hadorn, Y. Kawamura, Crystallographic classification of kink bands in an extruded Mg–Zn–Y alloy using intragranular misorientation axis analysis, Acta Mater 61 (2013) 2065–2076.
[44] K. Hagihara, T. Mayama, M. Honnami, M. Yamasaki, H. Izuno, T. Okamoto, T. Ohashi, T. Nakano, Y. Kawamura, Orientation dependence of the deformation kink band formation behavior in Zn single crystals, Inter. Jour. Plast. 77 (2016) 174–191.
[45] K. Hagihara, T. Okamoto, M. Yamasaki, Y. Kawamura, T. Nakano, Electron backscatter diffraction pattern analysis of the deformation band formed in the Mg-based long-period stacking ordered phase, Scrpta Mater 117 (2016) 32–36.
[46] T. Matsumoto, M. Yamasaki, K. Hagihara, Y. Kawamura, Configuration of dislocations in low-angle kink boundaries formed in a single crystalline long-period stacking ordered Mg-Zn-Y alloy, Acta Mater 151 (2018) 112–124.
[47] A. Inoue, K. Kishida, H. Inui, K. Hagihara, Compression of micro-pillars of a long period stacking ordered phase in the Mg-Zn-Y system, Mater. Res. Soc. Symp. Proc. 1516 (2013) 151–156.

[48] W.W. Jian, G.M. Cheng, W.Z. Xu, H. Yuan, M.H. Tsai, Q.D. Wang, C.C. Koch, Y.T. Zhu, S.N. Mathaudhu, Ultrastrong Mg alloy via nano-spaced stacking faults, Mater. Res. Lett. 1 (2013) 61–66.
[49] H. Pan, Q. Huang, G. Qin, H. Fu, M. Xu, Y. Ren, J. She, B. Song, B. Li, Activations of stacking faults in the calcium-containing magnesium alloys under compression, J. Alloys Comp. 692 (2017) 898–902.
[50] H. Wang, H. Geng, D. Zhou, K. Niitsu, O. Muransky, D. Zhang, Multiple strengthening mechanisms in high strength ultrafine-grained Al–Mg alloys, Mater. Sci. Eng. A 771 (2020) 138613.
[51] M. Ana, Q. Denga, Y. Lia, H. Song, M. Su, J. Cai, Molecular dynamics study of tension-compression asymmetry of nanocrystal α-Ti with stacking fault, Mater. Design 127 (2017) 204–214.
[52] R. Su, D. Neffati, J. Cho, Q. Li, J. Ding, H. Wang, Y. Kulkarni, X. Zhang, Phase transformation induced plasticity in high-strength hexagonal close packed Co with stacking faults, Scripta Mater 173 (2019) 32–36.
[53] K. Hagihara, T. Nakano, K. Sasaki, Anomalous strengthening behavior of Co–Cr–Mo alloy single crystals for biomedical applications, Scripta Mater 123 (2016) 149–153.
[54] K. Hagihara, K. Hayakawa, K. Miyoshi, Inducement of kink-band formation in directionally solidified Mg/$Mg_{17}Al_{12}$ eutectic alloy - Inspired by the deformation behavior of the long-period stacking ordered (LPSO) phase, Mater. Sci. Eng. A 798 (2020) 140087.
[55] https://www.mfs-materials.jp/en/.